# Journal of Materials Chemistry A

Accepted Manuscript


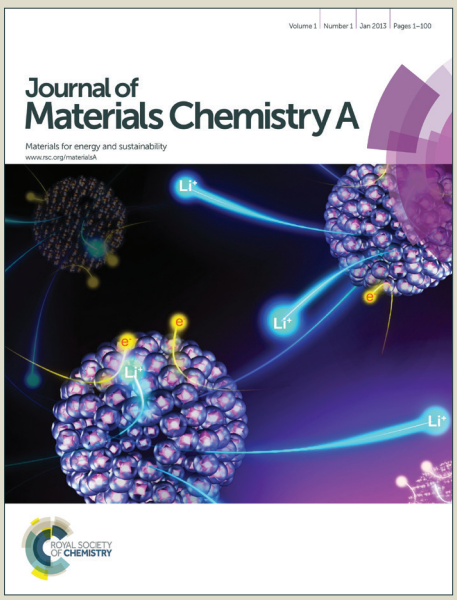





ROYAL SOCIETY OF CHEMISTRY

www.rsc.org/materialsA

Journal of
Materials Chemistry A

RSCPublishing

PAPER

# Firework-shaped $TiO_2$ microspheres embedded with few-layer $MoS_2$ as an anode material for excellent performance lithium-ion batteries

Bangjun Guo, Ke Yu,* Hao Fu, Qiqi Hua, Ruijuan Qi, Honglin Li, Haili Song, Shuang Guo and Ziqiang Zhu

Cite this: DOI: 10.1039/x0xx00000x

Received 00th January 2012,
Accepted 00th January 2012

DOI: 10.1039/x0xx00000x

www.rsc.org/

A three-dimensional porous hierarchical architecture of uniform $TiO_2$ microspheres embedded with $MoS_2$ nanosheets was prepared via a facile hydrothermal self-assembly scheme. A possible growth mechanism is presented in detail based on theoretical analysis and experimental facts. The further experiments demonstrate that $MoS_2$ nanosheets are uniformly coated on the surface of $TiO_2$ nanorods. Besides, the obtained F-$TiO_2$@$MoS_2$ possesses a large surface area and stable structure. Moreover, the F-$TiO_2$@$MoS_2$ microspheres were successfully assembled as an electrode material for lithium-ion batteries. As is expected, the electrochemical measurement demonstrates that the F-$TiO_2$@$MoS_2$ shows excellent electrochemical performance, which exhibits a high reversible capacity of 971 mA h $g^{-1}$ at a current density of 100 mA $g^{-1}$, markedly rate capability of over 450 mA h $g^{-1}$ at a current density of 1000 mA $g^{-1}$ and superior cycling stability of 714 mA h $g^{-1}$ after 200 cycles at a current density of 100 mA $g^{-1}$ as anodes material in LIBs.

## Introduction

Lithium-ion batteries (LIBs) with longer cycle life and higher power density have been regarded as one of the most promising power sources for the electric vehicles and hybrid electric vehicles.[1] Although widely used as a negative electrode material in commercial LIBs, graphite has a relatively low theoretical capacity and poor safety, and cannot meet the demand for large-scale batteries in the future.[2,3] Compared with bulky counterparts, nanomaterials can achieve better cyclability and higher specific capacity due to the large ionic contact area, decreased diffusion lengths and enhanced kinetics.[4,5] The enhanced electrochemical performances as anodes of nanomaterials are strongly dependent on their sizes, morphologies, and structures, which would provide high specific surface area, good mechanical properties, and fast mass and electron transport kinetics. However, owing to their high surface energy, nanoparticles tend to self-aggregate, accompanying with the process of $Li^+$ ion charge–discharge, which breaks down the conductive path among the active materials, conductive reagent and electrolyte, and gives rise to the fast fading in capacity upon extended cycling of LIBs.[6,7] So it is crucial to retain the large contact to fully fulfill the advantage of active nanomaterials. To solve the above problem, one feasible strategy is to design and prepare hollow, hierarchical and porous nanostructures. The ideal nanostructures are supposed to be three-dimensional (3D) porous stable building blocks as the skeleton which composed of various hierarchical structures with high specific surface area, which synergistically enhance the features of nanomaterials. In such kind of structures, the micrometer dimension of architectural skeleton effectively avoids aggregation of the active nanomaterials and promotes the kinetics of $Li^+$-ion storage due to the shortened diffusion paths of $Li^+$ ions. Meanwhile at such nanoscale, the primary architecture loaded on the skeleton facilitates the transport of electrons and ions.[8,9] Titanium dioxide ($TiO_2$), which possesses a low volume variation and display favourable cycling stability during the charge–discharge process, recently has received special interest for LIBs for several reasons.[10–14] Such as, $TiO_2$ anodes can efficiently avoid the formation of SEI (solid electrolyte interface) layers and dendritic lithium, which improves the safety of the batteries compared with carbon-based anodes.[15] What's more, $TiO_2$ is a fast and low voltage insertion host for Li. During the insertion/extraction of $Li^+$, $TiO_2$ can remain structurally stable and be free of electrochemical Li deposition, which is vital for the safe operation of LIBs. Thus far, many nanostructures of $TiO_2$ such as nanorods, nanoparticles and nanospheres have been reported for lithium storage.[16–18] Nevertheless, the cycling performance of $TiO_2$ electrodes at high charge–discharge rates is still poor owing to the poor electron transport and low $Li^+$-ion diffusivity in $TiO_2$. Although these $TiO_2$ nanostructures exhibit a long term cycling stability, the specific capacity is only 161.1 mA h $g^{-1}$,

which impedes their practical application as electrode materials for LIBs.[17] Therefore, constructing uniform hybrid structures of 3D $TiO_2$ with hierarchical structures and high specific surface area should be explored. For example $MoS_2$ nanosheets will effectively extra increase the electrode/electrolyte contact area and lowering the energy barrier for $Li^+$-ion movement.[19] The structure of $MoS_2$ is analogous to that of graphite, in which S–Mo–S layers are held together by van der Waals forces.[20] Such layered structure of $MoS_2$ facilitates reversible $Li^+$ intercalation/extraction, which enables $MoS_2$ nanosheets to be a good electrode material with high capacities up to 1000 mA h $g^{-1}$ for LIBs.[21-23] Through this way, $MoS_2$ nanosheets are evenly assembled on the surface of $TiO_2$ in the hybrid nanostructure of $TiO_2$@$MoS_2$. It is considered as a significant innovation for developing novel electrode materials with improved electrochemical performances. Thus far, one-dimensional (1D) nanostructured $TiO_2$ such as nanotubes and nanorods composed of $MoS_2$ nanosheets were evaluated as an anode material for LIBs.[24,25] However, only depending on the surface contact between 1D $TiO_2$ and $MoS_2$ nanosheets, composed nanostructures would also easily tend to self-aggregate during the process of $Li^+$ ion charge–discharge, which put a bar on their applications in LIBs. Here, we propose a novel strategy to fabricate firework-shaped $TiO_2$ microspheres embedded with few-layer $MoS_2$ (F-$TiO_2$@$MoS_2$) in a mild condition and use them as electrode materials for the first time. Such nanostructures of porous and hierarchical F-$TiO_2$@$MoS_2$ are expected to exhibit enhanced electrochemical performances, and to fulfill the advantage of both high reversible capacity and superior cycling stability. When such nanostructures evaluated as an anode material for LIBs, they shows remarkably improved electrochemical performance as high as 714 mA h $g^{-1}$ (100 mA $g^{-1}$, 200th cycle), compared with pure $MoS_2$ and $TiO_2$.

## Experimental

### Preparation of F-$TiO_2$

Three-dimensional firework-shaped $TiO_2$ microspheres were prepared under a mild hydrothermal process. Typically, 4 mL of tetrabutyl titanate (TBOT) and 2 mL of hydrochloric acid were mixed in a conical flask, and shaked it for 10 min to obtain a beige transparent solvent. Then 20 mL of oleic acid was doped slowly into the solvent and the mixture was kept stirring for 30 min. The resulting uniform mixed solvent was transferred into a 50 mL Teflon-lined stainless steel autoclave and hydrothermally treated at 180 ℃ for 4 h, then followed by natural cooling to room temperature for about 1 h. After the hydrothermal treatment, uniform F-$TiO_2$ microspheres were obtained. After cooling to room-temperature, the as-prepared samples were washed extensively with acetone and ethyl alcohol for several times until getting the clean white precipitate, and then dried at 60 ℃ for 12 h in air.

### Synthesis of firework-shaped $TiO_2$@$MoS_2$ microspheres

The as-prepared F-$TiO_2$ microspheres were embedded with $MoS_2$ nanosheets under another hydrothermal process. In a typical synthesis, 1 g of $TiO_2$ microspheres was first dispersed into 40 mL of deionized water by sonication for 1 h to obtain a milky dispersion. Then 0.4 g of oxalic acid was added into the dispersion and the mixture was kept stirring for 30 min as part A. 0.5 g of sodium molybdate ($Na_2MoO_4 \cdot 2H_2O$) and 0.8 g of thiourea were dissolved in 40 mL deionized water by stirring for 30 min as part B. Parts A and part B were then mixed under vigorous stirring. After 15 min, the resulting uniform suspension was transferred into a 100 mL Teflon-lined stainless steel autoclave and hydrothermally treated at 200 ℃ for 24 h. After the hydrothermal treatment, uniform F-$TiO_2$@$MoS_2$ microspheres were obtained. The black precipitate was collected by centrifugation, washed thoroughly with deionized water and ethanol, and dried at 60 ℃ for 12 h. The preparation process of $MoS_2$ nanoflowers is similar to the one used for F-$TiO_2$@$MoS_2$, with 0.4 g of oxalic acid, 1 g of sodium molybdate and 1.6 g of thiourea, and without the addition of $TiO_2$ microspheres. Scheme 1 illustrates synthetic process of the present work. The preparations of uniform F-$TiO_2$ microspheres, which assembled by $TiO_2$ nanorods, were based on the first hydrothermal synthesis process. Firstly，at the very beginning, tetrabutyl titanate was hydrolyzed into the solvent and formed lots of random titania nucleus at a relative low temperature. As time went on and temperature grown, the high concentration of titanium precursor resulted in the formation of many titania spheres which were considered as the seeds for the further growth of crystal. Secondly, at an even higher temperature, the selective adsorption of $Cl^-$ on the nucleus which gave rise to a repulsive force between the nanoneedle side walls, thus favouring the grain orientation growth of $TiO_2$ along the (001) plane and forming the initial $TiO_2$ nanoneedles.[26] Thirdly, as the reaction time extended and temperature went up to 180 ℃, under the selective adsorption of $Cl^-$ and the high acid condition, $TiO_2$ nanoneedles tended to growing on (001) plane as well as (110) plane which possess the lowest energy, and eventually took the shape of nanorods.[27] The radial assembly in a good geometrical match to the spherical structure, which could significantly minimize their surface area and reduce the total free energy. The as-obtained 3D F-$TiO_2$ architecture was evenly embedded with $MoS_2$ nanosheets through another hydrothermal synthesis process, resulting in the novel porous, hierarchical and stable nanostructures.

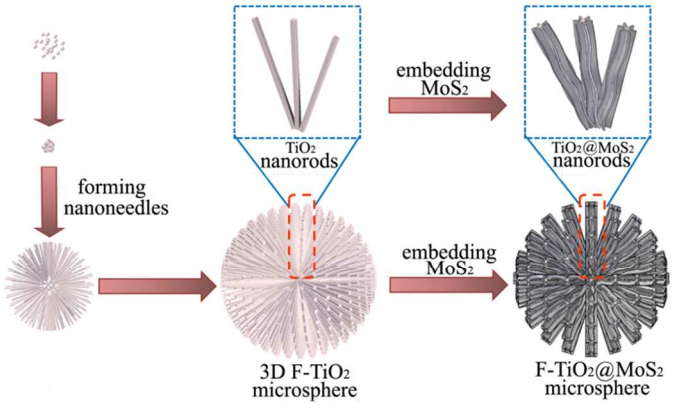


**Scheme 1.** Scheme for the fabrication of F-$TiO_2$@$MoS_2$.

### Characterizations

The crystal structure of the products was characterized by X-ray diffraction (XRD, Bruker D8 Advance diffractometer) with Cu Kα radiation (λ=1.5418 Å). Raman spectral experiments were carried out by a Jobin-Yvon LabRAM HR 800 micro-Raman spectrometer. A JEOL-2010 transmission electron microscope at an acceleration voltage of 200 kV, equipped with an energy dispersive X-ray analyzer (EDX) was used to investigate the transmission electron microscopy (TEM) images and chemical compositions of the samples. The field emission scanning electron microscopy (FE-SEM) images were taken on a JEOL-JSM-6700F SEM. Surface area determination was performed by Brunauer–Emmett–Teller (BET).

### Electrochemical measurements

All the electrochemical tests were carried out in a two-electrode coin-cell (CR 2025) which was assembled in an argon-filled glovebox ($O_2$ and $H_2O$ levels < 0.5 ppm). The as-prepared F-$TiO_2$@$MoS_2$, F-$TiO_2$ and $MoS_2$ nanoflowers were used as a working electrode, lithium foil as counter and reference electrodes, a polypropylene film (Celgard 2400) as a separator, and 1 mol $L^{-1}$ $LiPF_6$ dissolved in a mixture of ethylene carbonate (EC) and dimethyl carbonate (DMC) (v/v = 1 : 1) as an electrolyte. The working electrodes were prepared by a slurry tape casting procedure. The slurry consisted of 80 wt% active materials, 10 wt% carbon black and 10 wt% polyvinylidene fluoride (PVDF), dissolved in N-methyl-2-pyrrolidinone (NMP). The slurry was tape-cast on the copper foil, and then dried in a vacuum oven at 60 ℃ for 12 h. The charge–discharge cycles were carried out on the battery measurement system (LAND-CT2001A) at various current densities of 100–1000 mA $g^{-1}$ with a cutoff voltage range of 3.00 to 0.01 V versus $Li/Li^+$ at room temperature. Cyclic voltammetry measurements were carried out on a CHI660D electrochemical workstation over the potential range from 3.0 to 1.0 V at a scan rate of 0.5 mV $s^{-1}$.

## Results and discussion

The crystal structure of $MoS_2$ nanoflowers, F-$TiO_2$ and F-$TiO_2$@$MoS_2$ were characterized by using X-ray diffraction (Fig. 1a). It is clear that the pure $MoS_2$ nanoflowers (curve Ⅲ) and pure F-$TiO_2$ microspheres (curve Ⅱ) can be indexed to hexagonal phase of $MoS_2$ (JCPDS card no. 37-1492) and rutile phase of $TiO_2$ (JCPDS card no.21-1276) without any impurity. The XRD pattern for the F-$TiO_2$@$MoS_2$ is shown as the curve I, in which the distinct lattice planes correspond to the $MoS_2$ and $TiO_2$. It indicates that the F-$TiO_2$@$MoS_2$ hybrid structures are successfully obtained, and the F-$TiO_2$ microspheres are embedded with hexagonal phase of $MoS_2$ nanosheets. Diffraction peak at 14.3° corresponding to $MoS_2$ (002) plane in the patterns of F-$TiO_2$@$MoS_2$ which is much weaker than that in the patterns of $MoS_2$ nanoflowers, which might be because the anchored $TiO_2$ nanostructures prevent the $MoS_2$ nanosheets from restacking, substantially disrupting the flower-like nanostructure and forming the few-layer nanostructure.[28] To further explore the property of the hybrid nanostructure, the

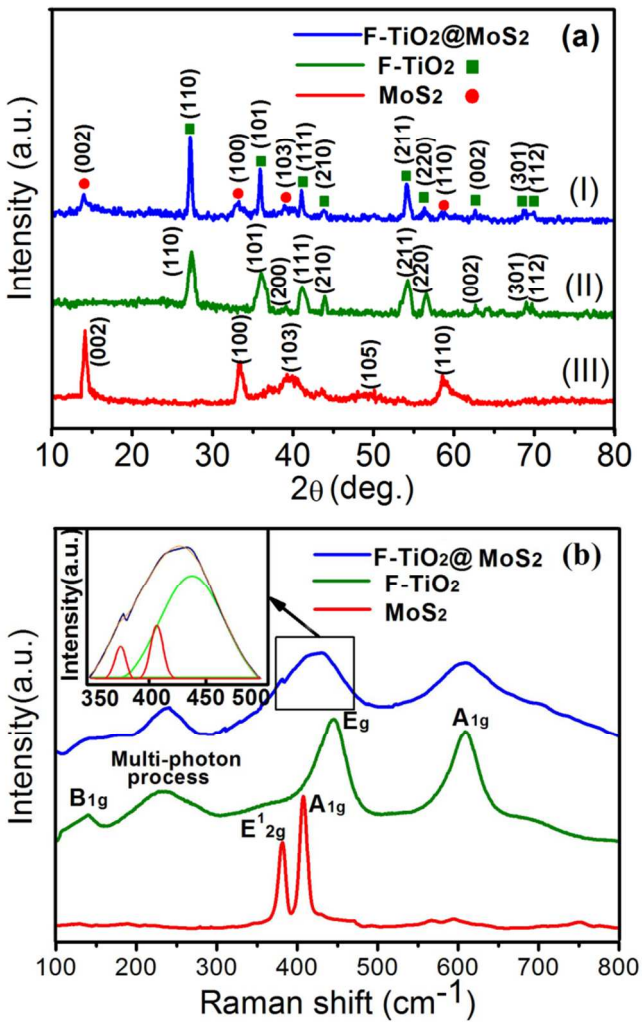


**Fig. 1** (a) XRD patterns and (b) Raman spectra of pure $MoS_2$ nanoflowers, pure F-$TiO_2$ microspheres and as-synthesized F-$TiO_2$@$MoS_2$ microspheres. Upper inset: Fitting Raman spectra of F-$TiO_2$@$MoS_2$.

phonon spectra of the $MoS_2$ nanoflowers, F-$TiO_2$ microspheres, and F-$TiO_2$@$MoS_2$ nanocomposite were measured by Raman scattering (Fig. 1b). The Raman phonon vibrational modes of pure F-$TiO_2$ microspheres at 140 $cm^{-1}$, 235 $cm^{-1}$, 445 $cm^{-1}$ and 608$cm^{-1}$ correspond to the $B_{1g}$, multi-photon process, $E_g$ and $A_{1g}$ modes of rutile $TiO_2$ respectively. Recently, Raman spectroscopy has also been used for the identification of few-layer $MoS_2$ nanosheets.[29,30] The two dominant Raman scattering peaks of pure $MoS_2$ observed at 380 $cm^{-1}$ and 407 $cm^{-1}$ can be assigned to $E^1_{2g}$ and $A_{1g}$ modes of the $MoS_2$ respectively. The $E^1_{2g}$ mode involves the in-layer displacement of Mo and S atoms, whereas the $A_{1g}$ mode involves the out-of-layer symmetric displacements of S atoms along the c axis.[31] In the Raman spectrum of the F-$TiO_2$@$MoS_2$ nanostructures, there is a blue shift observed in the mode of $B_{1g}$ compared to pure F-$TiO_2$ microspheres, which is mostly due to a surface strain induced by the coated $MoS_2$ nanosheets on the $TiO_2$ nanorods surface.[32] Meanwhile, there is also a broadened mixed peak observed at about 440 $cm^{-1}$. The fitting Raman spectra as shown in the inset of Fig. 1b indicates that this broadened peak

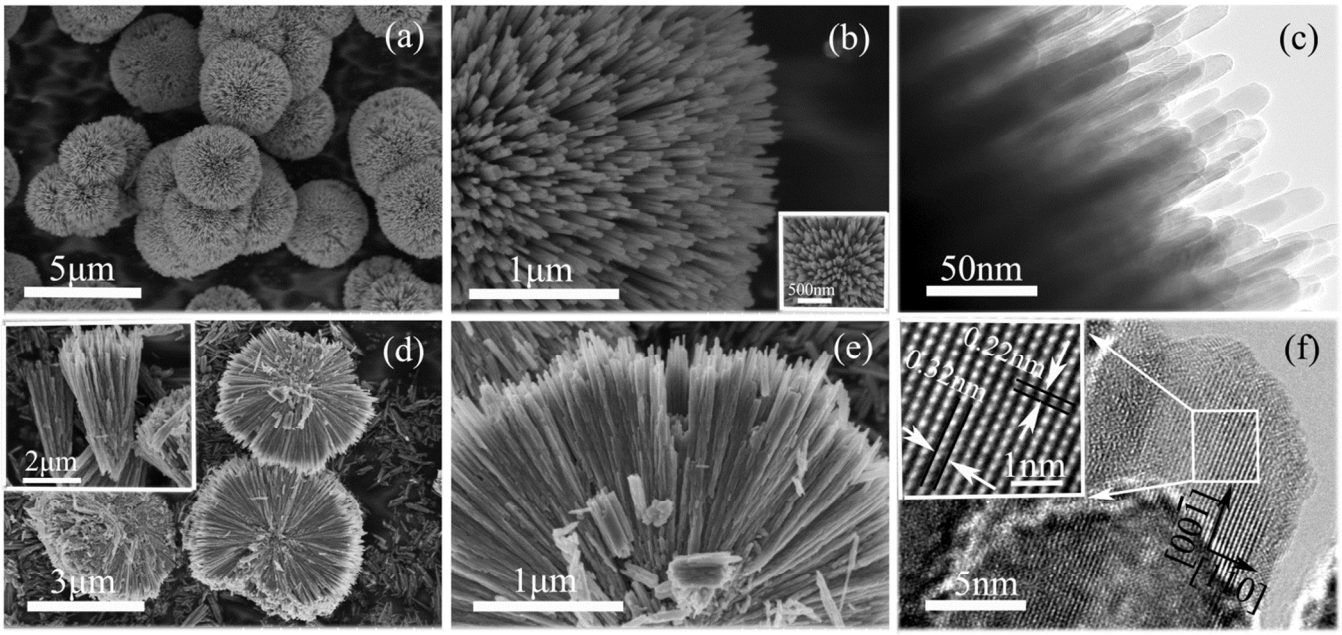


**Fig. 2** Firework-shaped $TiO_2$ microspheres. (a) Low magnification SEM image of $TiO_2$ microsphere. (b) High magnification SEM image of $TiO_2$ microsphere from the side view and the inset is the High magnification SEM image of $TiO_2$ microsphere from the front view. (c) TEM image of the surface of rutile $TiO_2$ microsphere. (d) Medium magnification SEM image of several broken $TiO_2$ microspheres and the upper inset is a bunch of $TiO_2$ nanorods. (e) High magnification SEM image of broken $TiO_2$ microsphere. (f) High-resolution TEM image of several $TiO_2$ nanorods and the upper inset is the HRTEM image corresponding to the rectangular area.

contains modes of $E^1_{2g}$ and $A_{1g}$ from $MoS_2$ nanosheets and modes of $E_g$ from F-$TiO_2$ microspheres with a red shift. These results further confirm the uniform composition of F-$TiO_2$@$MoS_2$. What's more, the shell configuration of $MoS_2$ nanosheets leads to a tensile strain along the [002] and a compressive strain in the basal plane. This tensile strain along [002] direction reduces the Van der Waals force between neighbouring layers, which causes a decrease in restoring force.[33] In terms of crystal structure, the phonon spectra of the hybrid structures confirm a composite configuration in our F-$TiO_2$@$MoS_2$ microspheres.

The morphology and structure of the products were characterized by SEM and TEM images. The nanostructures of F-$TiO_2$ microsphere with a diameter of ~ 4 μm are observed in the low magnification SEM, as shown in Fig. 2a. Fig. 2b and the inset of Fig. 2b clearly show the surfaces of these F-$TiO_2$ microspheres from the front and side view respectively. As can be seen from SEM images, firework-shaped $TiO_2$ is composed of homogeneous $TiO_2$ nanorods with numbers of mesoporous. Several broken microspheres further indicate that microspheres are composed of large quantities of elongated crystalline nanorods, which are closely packed (Fig. 2d). The inset of Fig. 2d shows a bunch of $TiO_2$ nanorods which is a part of the firework-shaped $TiO_2$ microsphere. It can be seen from the SEM figure that the formation of F-$TiO_2$ is by the stack of $TiO_2$ nanorods. What's more, it also could be observed that macropores were formed during the process of stack up. These macropores prove more space for the subsequent insertion of $MoS_2$ nanosheets. Fig. 2e displays the detail of this broken microsphere, it is from this morphology that, as also presented in the TEM image (Fig. 2c), nanorods with a mean length of ~700 nm and a width of ~30 nm, which forming the $TiO_2$ microsphere. The observation of nanostructures indicates that the formation of the three-dimensional firework-shaped nanostructure is possibly stemmed from the crystal growth of the primary nanoparticles and the further epitaxial process of these nanorods. The TEM image further displays the surface morphology of F-$TiO_2$ that the uniform $TiO_2$ nanorods make up the microsphere (Fig. 2c), which corresponds to the observation of SEM images. Moreover, the lattice fringes of $TiO_2$ in Fig. 2f are found to be about 0.32 nm and 0.22 nm respectively, corresponding to the $d_{110}$-spacings and $d_{100}$-spacings in the XRD pattern. Theoretical calculation shows that for a rutile $TiO_2$ lattice, the surface energy is $E_{(110)} < E_{(100)} < E_{(101)} < E_{(001)}$, for this nanostructure, $TiO_2$ grain growth is suppressed in the [001] direction and accelerated in the [110] direction, thereby forming the rod-like structure.[34] Fig. 3 shows the SEM images of $MoS_2$ nanoflowers. As can be seen from Fig. 3a, pure $MoS_2$

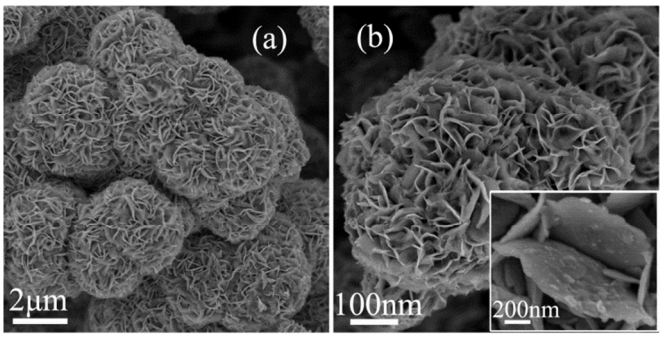


**Fig. 3** $MoS_2$ nanoflowers. (a) Low magnification SEM image of $MoS_2$ nanoflowers. (b) Medium magnification SEM image of $MoS_2$ nanoflowers. (c) High magnification SEM image of $MoS_2$ nanoflowers.

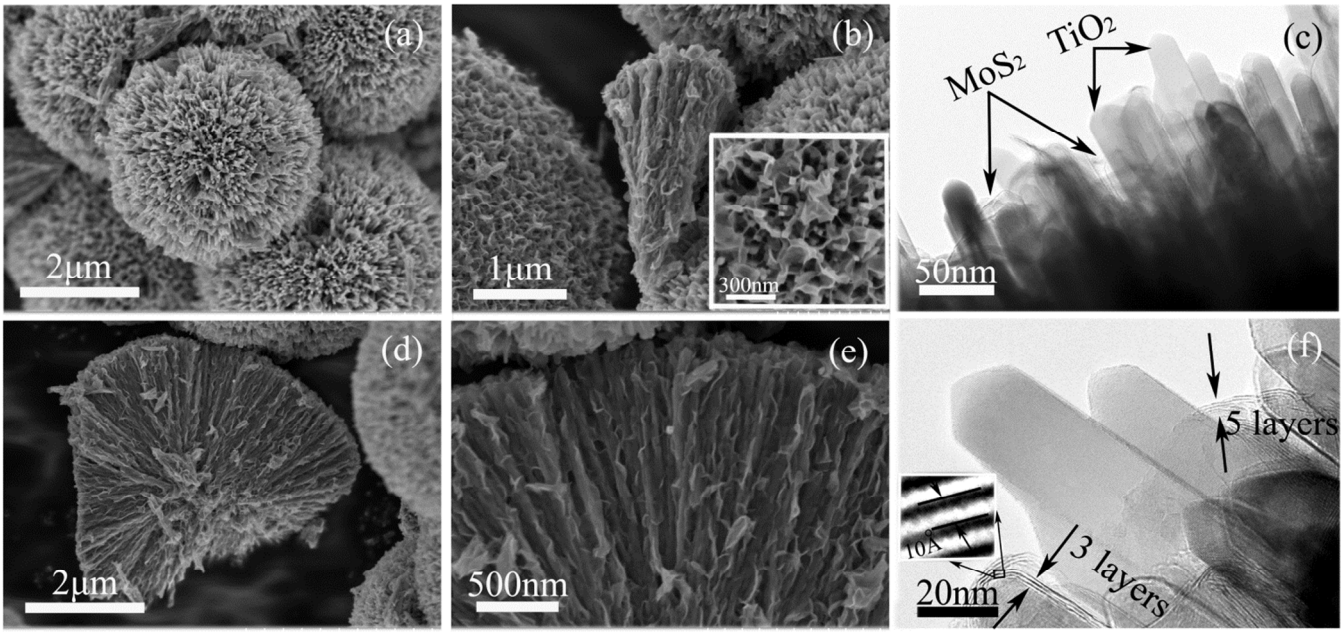


**Fig. 4** Firework-shaped $TiO_2$@$MoS_2$ microspheres. (a) Medium magnification SEM image of F-$TiO_2$@$MoS_2$ microsphere. (b) High magnification SEM image of fan-shaped F-$TiO_2$@$MoS_2$ microstructure and the inset is the High magnification SEM image of F-$TiO_2$@$MoS_2$ microsphere from the front view. (c) TEM image of the surface of F-$TiO_2$@$MoS_2$ microsphere. (d) Medium magnification SEM image of broken F-$TiO_2$@$MoS_2$ microspheres (e) High magnification SEM image of broken F-$TiO_2$@$MoS_2$ microsphere. (f) High-resolution TEM image of F-$TiO_2$@$MoS_2$.

nanoflower has an average diameter of ~2 μ m. It also could be observed clearly that the surface of the nanoflower with a large amount of petals, which are tightly aggregated. From the Fig. 3b, medium magnification of a single $MoS_2$ nanoflower shows that the $MoS_2$ nanopetals aligned together in a disordered manner with considerable interspace pointing towards a common inner center to form the spherical product.[35] Fig. 3c further shows the detail of $MoS_2$ nanopetals.

Fig. 4a shows the SEM images of the F-$TiO_2$@$MoS_2$ microspheres after another hydrothermal synthesis process. It can be seen from the SEM image that almost every F-$TiO_2$ microsphere is successfully and uniformly embedded with $MoS_2$ nanosheets (Fig. 4a), which can be put down to the assistant function of oxalic acid and thiourea.[36] After acidification process, the surface of $TiO_2$ becoming rough and the distance between nanorods enlarged, which provide more contact area and space for the composition of $MoS_2$ nanosheets. As can be seen from the inset of Fig. 4b, F-$TiO_2$ is uniformly embedded with few-layer $MoS_2$ on the surface from the front view. A broken microsphere of F-$TiO_2$@$MoS_2$ is depicted in Fig. 4d shows that apertures of $TiO_2$ microsphere are uniformly filled with $MoS_2$ nanosheets. Fig. 4e further reveals that the distribution of $MoS_2$ nanosheets is homogeneous not only on the central pore of F-$TiO_2$, but also on the surface of $TiO_2$ nanorods. Fig. 4c presents the TEM image of the surface of F-$TiO_2$@$MoS_2$. It could be clearly observed that $MoS_2$ nanosheets are equably assembled into the mesoporous of F-$TiO_2$. The HRTEM image of F-$TiO_2$@$MoS_2$ displayed in Fig. 4f also shows that F-$TiO_2$ is encased of several layers of $MoS_2$ tightly. It also indicates that the pure $MoS_2$ nanosheets are very thin compared with the initial $MoS_2$ nanoflowers. Details also reveal

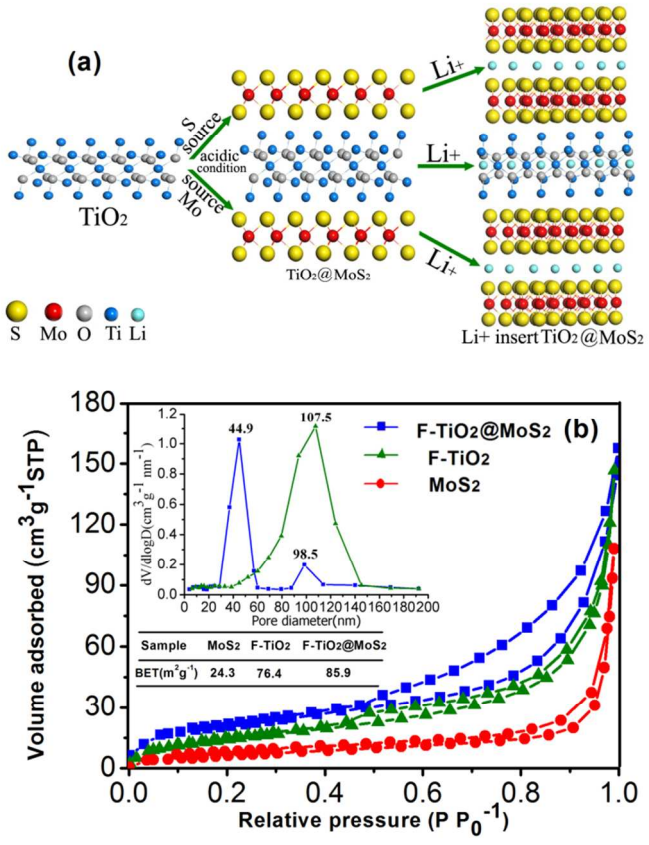


**Fig. 5** (a) Schematic illustration for fabricating F-$TiO_2$@$MoS_2$ microspheres and the process of the subsequent insertion of $Li^+$. (b) $N_2$ adsorption–desorption isotherm of the F-$TiO_2$@$MoS_2$ microspheres and the inset is pore size distribution.

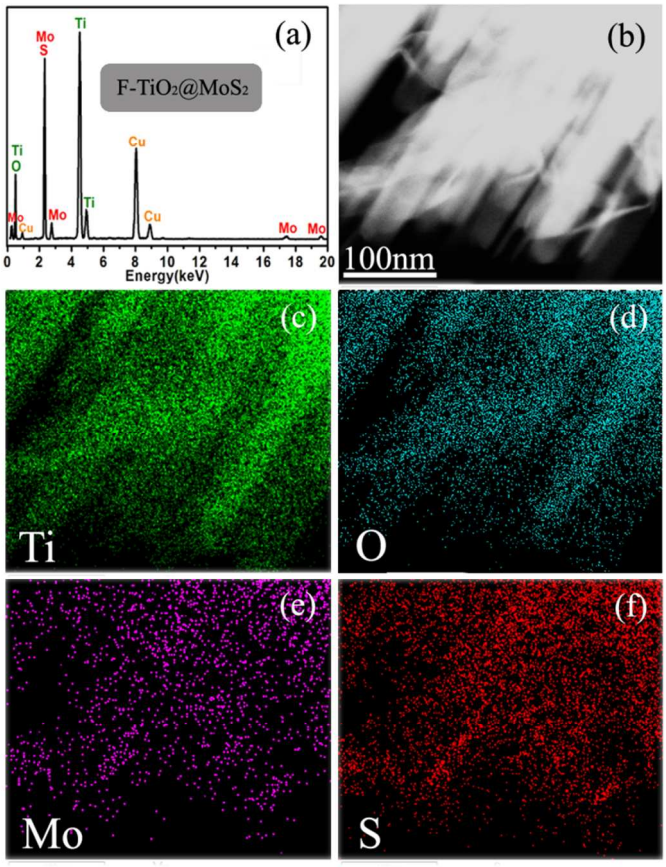


**Fig. 6** (a) EDS spectrum of the F-$TiO_2$@$MoS_2$ microsphere. (b) Scanning transmission electron microscopy (STEM) image of F-$TiO_2$@$MoS_2$ microstructure. (c-f) the corresponding EDX mapping images of titanium, oxygen, molybdenum and sulphur elements.

that, some part of the $MoS_2$ nanosheets are even 3 or 5 layers on the region of $TiO_2$ nanorods surface. These separated $MoS_2$ nanosheets are not only covered on the surface of $TiO_2$ nanorods but also embedded into the voids between $TiO_2$ nanorods. It is worth noticing from the inset of Fig. 4f that some of the interlayer distances of $MoS_2$ nanosheets are enlarged from 6.2 Å to 10 Å with the intercalation into $TiO_2$ microsphere, which causes a decrease in restoring force and complies with the Raman and XRD observation. What's more, the enlarged interlayer distances of $MoS_2$ nanosheets are also providing more space for the storage of $Li^+$ ions. The particular of Fig. 4f shows the lattice fringes of $TiO_2$ nanorods and $MoS_2$ nanosheets, which suggests the well-defined crystal structure of our as-synthesized F-$TiO_2$@$MoS_2$ composite nanostructure.

Fig. 5a shows the composite procedure for the F-$TiO_2$@$MoS_2$ microspheres and the process of the subsequent insertion of $Li^+$. The firework-shaped $TiO_2$ microspheres are assembled by uniform $TiO_2$ nanorods. After acid treatment, the surface of $TiO_2$ nanorods becomes rough, which provides high energy nucleation sites for the growth of $MoS_2$ nanosheets. During the $Li^+$ intercalation process, $Li^+$ insert into not only the $MoS_2$ nanosheets but also the $TiO_2$ nanorods, such action makes a contribution to the improvement of rate capability for LIBs. The nitrogen isothermal adsorption technique was employed to further investigate the specific surface areas of the obtained samples, and the results are shown in Fig. 5b. The Brunauer–Emmett–Teller (BET) specific surface area of the $MoS_2$ nanoflowers is 24.3 $m^2$ $g^{-1}$. Meanwhile, the specific surface area of F-$TiO_2$@$MoS_2$ microsphere is 85.9 $m^2$ $g^{-1}$, which even higher than that of firework-shaped $TiO_2$ (76.4 $m^2$ $g^{-1}$). Considering the morphology of the F-$TiO_2$@$MoS_2$ sample observed in the SEM images, such high specific surface areas and the mesoporous feature could be attributed to the interparticle space, which is caused by the disordered insertion of $MoS_2$ nanosheets and ordered stacking $TiO_2$ nanorods.[37] The pore size distribution of pure F-$TiO_2$ and F-$TiO_2$@$MoS_2$ microspheres were derived from the BJH method is shown in the inset of Fig. 5b. The peak at 107.5 nm of F-$TiO_2$ microspheres is attributed to the forming of macropores which were stacked up by $TiO_2$ nanorods. For the F-$TiO_2$@$MoS_2$ microsphere, the sharp peak at 44.9 nm corresponds to mesoporous in F-$TiO_2$@$MoS_2$ microsphere architectures. Besides, the weak peak at 98.5 nm is also attributed to the forming of macropores. Such a high specific surface area of F-$TiO_2$@$MoS_2$ microspheres with massive mesopores and macropores could be desirable for energy storage application.

In order to investigate the detailed local elemental composition and distribution of the as-formed F-$TiO_2$@$MoS_2$ composite, energy dispersive X-ray (EDX) mapping analysis and scanning transmission electron microscopy (STEM) are carried out. Fig. 6a shows the energy-dispersive spectrometry (EDS) analysis of a portion of the as-prepared F-$TiO_2$@$MoS_2$ that the composite mainly contains Mo, S, Ti and O. It can be seen from Fig. 6b that a typical STEM image of the F-$TiO_2$@$MoS_2$ is revealed. From the elemental mapping, it can be observed that the Ti and O elemental distribution shows quite unique behaviour and those rod-shaped areas have strong Ti and O signal, which indicates that the formed $TiO_2$ nanorods are restricted to those areas (Fig. 6c-d). For the Mo and S signals, the distinct distribution of each signal clearly shows the agglomerate of $MoS_2$ nanosheets on the surface of $TiO_2$ nanorods which corresponds to the observation of STEM image (Fig. 6e-f). The above analysis is verified that our method is an effective strategy to produce a high quality of porous, hierarchical and stable F-$TiO_2$@$MoS_2$ nanostructures. The plentiful accessible $MoS_2$ nanosheets would drastically alter the electronic performance of F-$TiO_2$, offer more active sites for lithium storage, effectively improve lithium transportation kinetics, thus enhancing the rate performance and cycling stability.[38]

To demonstrate the electrochemical properties of the as-prepared composition on the $Li^+$ insertion/extraction properties, we assembled $MoS_2$ nanoflower, F-$TiO_2$ microsphere and F-$TiO_2$@$MoS_2$ microsphere electrodes as potential anode materials for high power LIBs. Fig. 7 shows the typical cyclic voltammograms (CVs) of the pure $MoS_2$, pure F-$TiO_2$ and F-$TiO_2$@$MoS_2$ electrode for the first, second and fifth cycles in the voltage range from 0.01 V to 3.0 V at a scan rate of 0.5 mV $s^{-1}$. It is observed from Fig. 7a that the CV behaviour of F-$TiO_2$@$MoS_2$ is generally including pure $MoS_2$ and pure F-$TiO_2$ nanostructures reported previously.[14,39,40,41] In the first cycle, the peak at 0.78 V corresponds to the phase transition of the

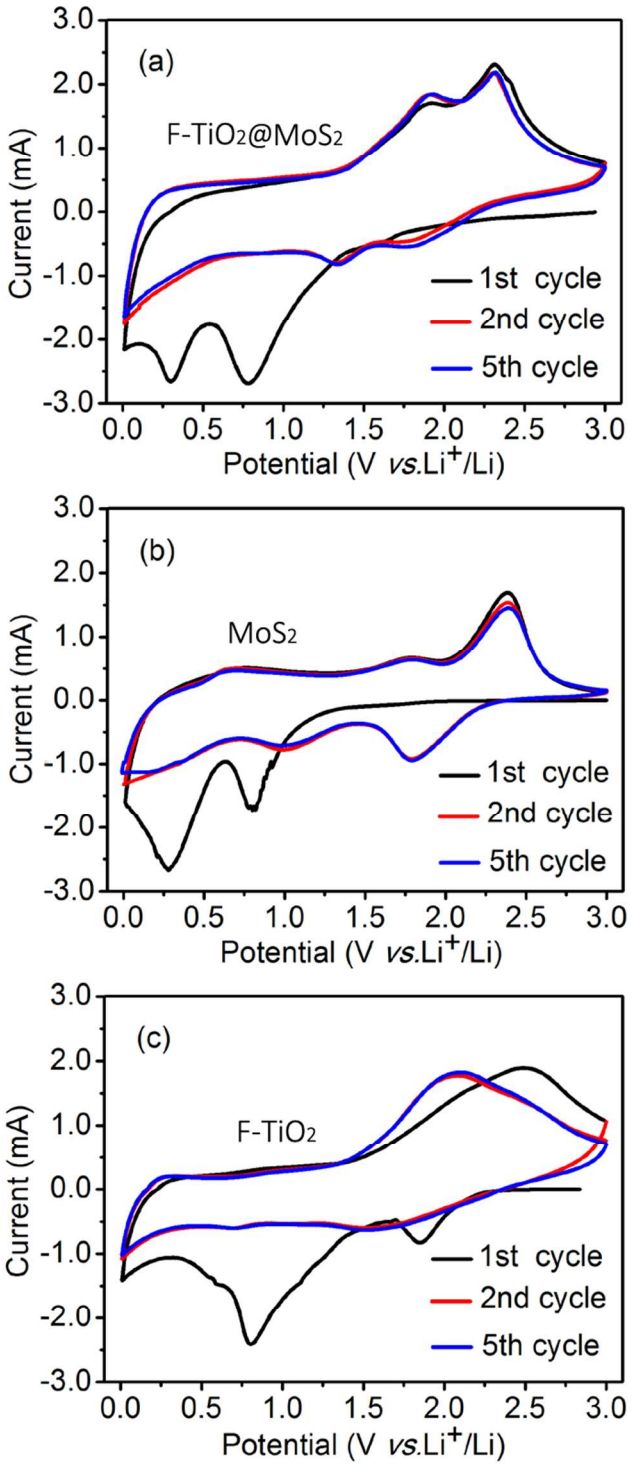


**Fig. 7** Cyclic voltammetry curves of F-$TiO_2$@$MoS_2$, pure $MoS_2$ and pure $TiO_2$ samples measured at a scan rate of 0.5 mV $s^{-1}$ in the voltage range of 0.01V–3 V (vs. $Li/Li^+$): (a) F-$TiO_2$@$MoS_2$; (b) $MoS_2$ and (c) $TiO_2$.

$MoS_2$ from trigonal prismatic to octahedral, which attributed to intercalation of $Li^+$ ions into the $MoS_2$ lattice.[42,43] This peak moves lower compared with the $MoS_2$. It could be explained as that the existence of $TiO_2$ nanorods separating $MoS_2$ from nanoflowers into few-layer nanosheets, which makes the speed of phase transition more quickly and transform drastically. This pronounced peak disappears in the successive discharge processes for few amorphous $MoS_2$ lattices are reformed after the first charge process. A shoulder appears at 0.54 V before reaching the next peak, which can be described to the formation of a gel-like solid electrolyte interface layer caused by the electrochemically driven electrolyte decomposition.[44] The sharp peak which located at 0.3 V is attributed to the complete reduction process of $MoS_2$ into Mo nanoparticles embedded in a $Li_2S$ matrix, which is based on the conversion reaction: $MoS_2 + 4Li^+ + 4e^- \rightarrow Mo + 2Li_2S$.[45] In the successive discharge cycles, the reduction peaks which are observed at 0.3 V and 0.78 V are replaced by a new peak at 1.33 V. This conspicuous change in the CV details between the first and subsequent discharges is in keeping with the previous reports, indicating that $MoS_2$ experiences an irreversible phase transition in the initial discharge.[46] Moreover, during the subsequent cathodic scans, a new broad peak appears at 1.69 V, which is corresponding to the presence of a multi-step lithium insertion mechanism.[21,37] In the anodic scan, there is an oxidation peaks at 2.3 V with few change in the subsequent sweeps, corresponding to the lithium extraction process and the transformation of Mo to $MoS_2$. In addition, a pair of new peaks turns up at 1.33 V and 1.9 V in the cathodic and anodic sweep which can be fined during the 2nd and 5th discharge processes respectively. This change can be interpreted as the lithiation process of S to form $Li_2S$: $S + Li^+ + 2e^- \leftrightarrow Li_2S$, as well as synergy effect of the reduction $Ti^{4+}$ into $Ti^{3+}$ during the cathodic scan and subsequent oxidation to $Ti^{4+}$ during the anodic scan which is based on the conversion reaction: $TiO_2 + x(Li^+ + e^-) \leftrightarrow Li_xTiO_2$ ($0 < X < 1$). These results illustrate that the $TiO_2$ nanostructures also make a contribution to the charge-discharge capacity. Nevertheless, it suggests that the $MoS_2$ nanosheets which makes the major contribution to the reversible capacity. As shown in Fig. 7b, the $MoS_2$ electrode demonstrates the similar peak position to that of F-$TiO_2$@$MoS_2$. However, the oxidation peaks of F-$TiO_2$@$MoS_2$ are higher than that of $MoS_2$ which could be explained as the combined action of $MoS_2$ and F-$TiO_2$, as well as the reduced $MoS_2$ layers works more effectively during the oxidation process. What's more, the CV behaviour of F-$TiO_2$ is shown in Fig. 7c, peaks position are also can be included in that of F-$TiO_2$@$MoS_2$. It is obvious that F-$TiO_2$ with poor electron transport exhibits much degraded electrochemical activity and reversibility for $Li^+$ storage.

Fig. 8a displays the discharge-charge curves in the first three, 10th, 50th, 100th, 150th and 200th cycles of the F-$TiO_2$@$MoS_2$ microspheres, measured at a current density of 100 mA $g^{-1}$ between 0.01 V and 3.0 V. In agreement with the above CV study, two plateaus at 0.8 V and 0.3 V are observed in the first discharge process, which respectively correspond to the phase transition of $MoS_2$ from trigonal prismatic to octahedral and the conversion reaction process, in which $Li_xMoS_2$ was completely decomposed into Mo nanoparticles embedded in a $Li_2S$ matrix. In subsequent discharge curves, the plateaus in the first discharge are disappeared, while two plateaus at 1.8 V and 1.4 V are appeared, which are corresponding to a multi-step lithium

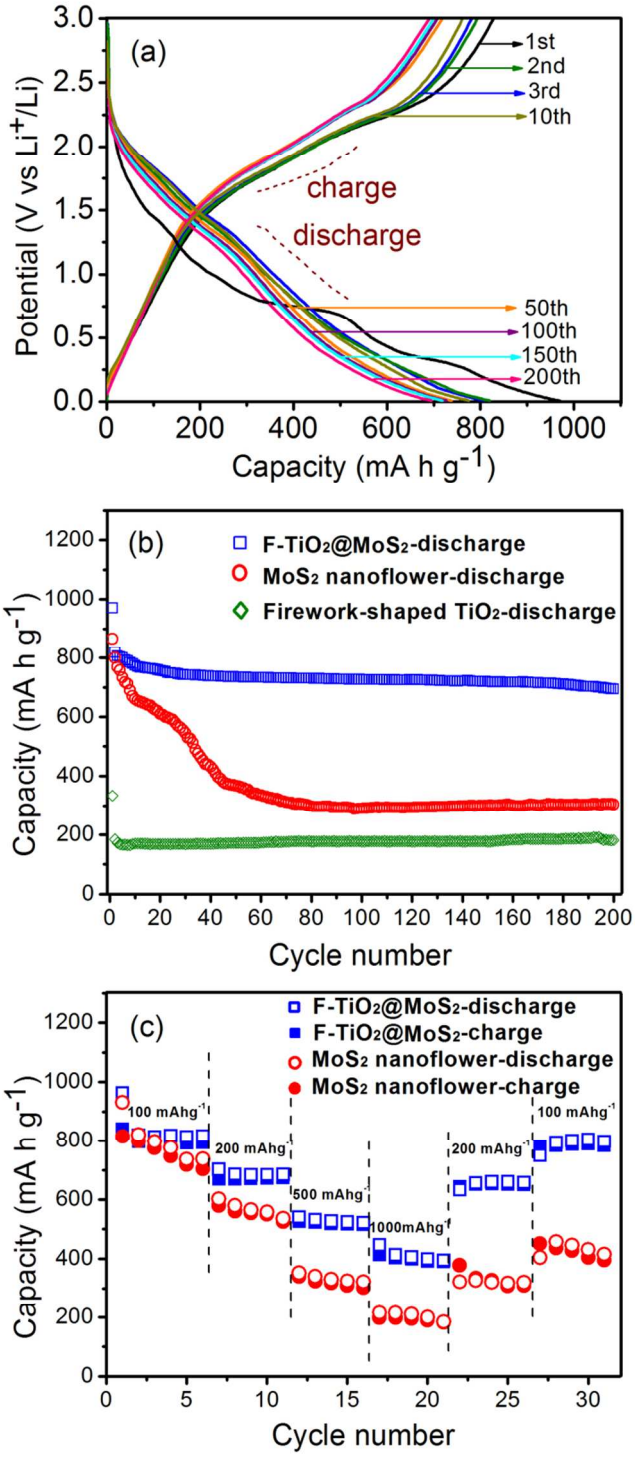


**Fig. 8** (a) Charge–discharge voltage profiles at a current density of 100 mA $g^{-1}$ of F-$TiO_2$@$MoS_2$ microspheres. (b) Comparative cycling performance of pure $MoS_2$, F-$TiO_2$@$MoS_2$ and pure $TiO_2$ at a current density of 100 mA $g^{-1}$. (c) Rate performance of F-$TiO_2$@$MoS_2$ microspheres and pure $MoS_2$ nanoflowers at different current densities.

insertion processes. During the charge process, conspicuous potential plateau at about 2.4 V is noticed, which is also in accordance with the previous CV curves. In the first cycle, the F-$TiO_2$@$MoS_2$ reveals a considerable discharge and charge

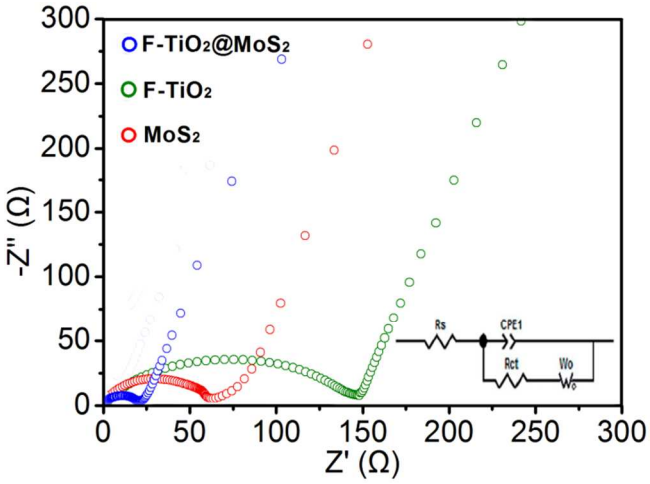


**Fig. 9** Nyquist plots of the F-$TiO_2$@$MoS_2$, pure $MoS_2$ and F-$TiO_2$ electrodes in the frequency range from 100 kHz to 0.01 kHz.

capacities of 971 mA h $g^{-1}$ and 828 mA h $g^{-1}$ respectively, which is attributed to the uniformly embedding $MoS_2$ nanosheets into F-$TiO_2$ which store more lithium ions on the surface region. For the rest of the early discharge-charge cycles, the specific capacity is remained at a high level of 819mA h $g^{-1}$ (2nd discharge), 793 mA h $g^{-1}$ (2nd charge) and 807 mA h $g^{-1}$ (3rd discharge), 781 mA h $g^{-1}$ (3rd charge), respectively. Besides possesses higher specific capacity in the initial cycle, the F-$TiO_2$@$MoS_2$ microspheres also shows better cycling performance of 735 mA h $g^{-1}$ (50th discharge) and 728 mA h $g^{-1}$ (50th charge), 726 mA h $g^{-1}$ (100th discharge) and 720 mA h $g^{-1}$ (100th charge), 719 mA h $g^{-1}$ (150th discharge) and 715 mA h $g^{-1}$ (150th charge), 714 mA h $g^{-1}$ (200th discharge) and 712 mA h $g^{-1}$ (200th charge), with a Coulombic efficiency is about 100%.

The cycling performance of the as-synthesized F-$TiO_2$@$MoS_2$ as well as and pure $MoS_2$ nanoflowers and F-$TiO_2$ microspheres were evaluated at a discharge current density of 100 mA $g^{-1}$ as shown in Fig. 8b. The $MoS_2$ nanoflowers electrode delivers a diminishing discharge capacity from over 850 mA h $g^{-1}$ during initial cycles to 295mA h $g^{-1}$ at the 200th cycle with a capacity retention of 34.7%. In the meantime, the firework-shaped $TiO_2$ exhibited excellent cycling stability, while only a capacity of 177.5 mA h $g^{-1}$ is maintained after 200 cycles. When embedding $MoS_2$ nanosheets into F-$TiO_2$ microspheres, the cyclic stability and discharge capacity of these composites have been notably improved. It is very remarkable that the F-$TiO_2$@$MoS_2$ electrode displays an extraordinary capacity of 820 mA h $g^{-1}$ in the first few cycles and the capacity can still maintain at 714 mA h $g^{-1}$ after 200 cycles, which indicates a low average capacity fading of 0.07% per cycle, as shown in Table 1. It is worth mentioning that the reversible capacity and cyclability of F-$TiO_2$@$MoS_2$ are higher than most previously reported $MoS_2$-based anodes.[40, 47, 48] Apart from the high reversible capacity and good cycling behaviour, F-$TiO_2$@$MoS_2$ also exhibits excellent rate capability. Fig. 8c compares the rate capability of F-$TiO_2$@$MoS_2$ microspheres with pure $MoS_2$ nanoflowers. The 3D microsphere of F-TiO2@MoS2 electrode delivers a reversible discharge capacity

**Table 1** Comparison of cycling performance of F-$TiO_2$@$MoS_2$, pure F-$TiO_2$ and pure $MoS_2$.

| | 1st cycle capacity (mA h $g^{-1}$) | 200th cycle capacity (mA h $g^{-1}$) | capacity retention ( %) |
|---|---|---|---|
| $MoS_2$ | 850 | 295 | 34.7 |
| F-$TiO_2$ | 324 | 177.5 | 54.8 |
| F-$TiO_2$@$MoS_2$ | 820 | 714 | 87 |

of 962 mA h $g^{-1}$ at a current density of 100 mA $g^{-1}$ in the first cycle, and retains a capacity of around 450 mA h $g^{-1}$ as the current density increases to 1000 mA $g^{-1}$. After cycling under high current densities, the current density decrease to 200 mA $g^{-1}$ and 100 mA $g^{-1}$, the F-$TiO_2$@$MoS_2$ can still respectively regain a discharge capacity near 660 mA h $g^{-1}$ and 805 mA h $g^{-1}$. However, for the $MoS_2$ nanoflowers, the discharge capacity decays to less than 200 mA h $g^{-1}$ as the current density is 1000 mA $g^{-1}$, and remanent discharge capacity (410 mA h $g^{-1}$) only around 45% of the initial discharge capacity (910 mA h $g^{-1}$), when the current density declines to 100 mA $g^{-1}$. It is further proof that the F-$TiO_2$@$MoS_2$ microspheres exhibit much improved rate capability and cyclic capacity retention.

The electrochemical impedance spectra (EIS) of pure $MoS_2$ nanoflower, F-$TiO_2$ microsphere and F-$TiO_2$@$MoS_2$ microsphere electrodes are compared in Fig. 9. In the three Nyquist plots, the electrodes exhibits a semicircle at high frequencies representing charge-transfer resistance and a straight sloping line at low in association with the Warburg diffusion of $Li^+$ ions to the bulk of the active material. The equivalent circuit for the AC impedance spectra is represented in the inset of Fig. 9. The diameter of the semicircle at high frequencies region is signally reduced in the plot of F-$TiO_2$@$MoS_2$, compared with that of pure $MoS_2$ nanoflower and F-$TiO_2$ microsphere. It seemed that the composite F-$TiO_2$@$MoS_2$ structure can effectively facilitate the transportation of $Li^+$ ions and enhance the conductivity of electrode.[49] The rationally designed 3D porous hierarchical firework-shaped $TiO_2$ embedded with $MoS_2$ nanosheets is confirmed that can achieve excellent cycling performance as well as high capacity and rate capability, which could be explained as follows. Firstly, the F-$TiO_2$ microspheres can be taken for the skeleton, which effectively mitigates the stress and volume change accompanying the process of $Li^+$ ion charge-discharge process. Additionally, the voids which are formed after the insetting of $MoS_2$ nanosheets also buffer the volume change, as a result, the cycling performance of the F-$TiO_2$@$MoS_2$ is greatly improved. Secondly, compared with $MoS_2$ nanoflowers, such few-layer $MoS_2$ nanosheets provides numerous open channels for the access of electrolyte and shortens the diffusion paths of $Li^+$ ions, thus improving the dynamic performance of $Li^+$ storage. Finally, the $MoS_2$ nanosheets are distributed dispersedly on the surface of $TiO_2$ nanorods which enlarge the contact area between the building blocks and the electrolyte, thus offering more active sites for $Li^+$ insertion/distraction, resulting in high capacity and rate capability.

## Conclusions

In summary, a facile strategy for fabricating hierarchically porous rutile firework-shaped $TiO_2$ microspheres embedded with $MoS_2$ nanosheets was developed. In this composite nanostructure, porous stable F-$TiO_2$ works as skeleton embedded with hierarchical few-layer $MoS_2$ with high specific surface area, which synergistically enhance the features of nanomaterial. The morphology of F-$TiO_2$@$MoS_2$ is further confirmed that $MoS_2$ nanosheets are uniformly covered on the surface of $TiO_2$ nanorods which make up the F-$TiO_2$ microsphere, and few-layer $MoS_2$ also embedded into the mesoporous of F-$TiO_2$ microsphere which distribute between the $TiO_2$ nanorods. The as-obtained F-$TiO_2$@$MoS_2$ microspheres also exhibit greatly improved $Li^+$ storage properties with higher specific capacity, good rate performances and superior cycling performance, owing to the novel nanostructure. Our achieved results clearly demonstrate that the feasibility of F-$TiO_2$@$MoS_2$ can be used as anode materials for high performance LIBs in the future.

## Acknowledgements

The authors acknowledge financial support from the NSF of China (Grant Nos. 61274014, 61474043, 61425004), Innovation Research Project of Shanghai Education Commission (Grant No. 13zz033), and Project of Key Laboratory of Polar Materials and Devices (Grant No. KFKT2014003).

## Notes and references

*Key Laboratory of Polar Materials and Devices (Ministry of Education of China), Department of Electronic Engineering, East China Normal University, Shanghai, 200241, P. R. China. Fax: +86-21-54345198; Tel: +86-21-54345198; E-mail: yk5188@263.net*

1. P. G. Bruce, B. Scrosati and J. M. Tarascon, Angew. Chem. Int. Ed., 2008, 47, 2930.
2. M. Armand and J. M. Tarascon, Nature, 2008, 451, 652.
3. K. Kang, Y. S. Meng, J. Breger, C. P. Grey and G. Ceder, Science, 2006, 311, 977–980.
4. H. Li, Z. X. Wang, L. Q. Chen, X. J. Huang, Adv. Mater., 2009, 21,4593.
5. J. Chen, F. Y. Cheng, Accounts Chem. Res., 2009, 42, 713.
6. Y. S. Hu, P. Adelhelm, B. M. Smarsly, S. Hore, M. Antonietti,J. Maier, Adv. Funct. Mater., 2007, 17, 1873.
7. A. Magasinski, P. Dixon, B. Hertzberg, A. Kvit, J. Ayala, G. Yushin, Nat. Mater., 2010,9, 353.
8. L.C. Yang, S. N. Wang, J. J. Mao, J. W. Deng, Q. S. Gao,Y. Tang and O. G. Schmidt, Adv. Mater., 2013, 25, 1180–1184.
9. L. Q. Mai, F. Yang, Y. L. Zhao, X. Xu, L. Xu and Y. Z. Luo, Nat. Commun., 2011, 2, 5.
10. Y. P. Tang, D. Q. Wu, S. Chen, F. Zhang, J. P. Jia and X. L. Feng, Energy Environ. Sci., 2013, 6, 2447.
11. A. R. Armstrong, G. Armstrong, J. Canales, P. G. Bruce, Angew. Chem. Int. Ed., 2004, 43, 2286 – 2288.
12. Y. S. Hu, L. Kienle, Y. G. Guo and J. Maier, Adv. Mater., 2006, 18, 1421–1426.
13. M. Wagemaker, A. P. M. Kentgens and F. M. Mulder, Nature 2002, 418,397–399.
14. S. H. Liu, Z. Y. Wang, C. Yu, H. B. Wu, G. Wang, Q. Dong, J. S. Qiu, A. Eychmuller and X. W. Lou, Adv. Mater., 2013,25, 3462.
15. S. X. Yu, L. W. Yang, Y. Tian, P. Yang, F. Jiang, S. W. Hu, X. L. Wei and

J. X. Zhong, J. Mater. Chem. A, 2013, 1, 12750.
16. Y. M. Jiang, K. X. Wang, X. X. Guo, X. Wei, J. F. Wang and J. S. Chen, J. Power Sources, 2012, 214, 298.
17. J. S. Chen and X. W. Lou, J. Power Sources, 2010, 195, 2905.
18. T. B. Lan, Y. B. Liu, J. Dou, Z. S. Hong and M. D. Wei, J. Mater. Chem. A, 2014, 2, 1102.
19. Q. Gao, C. Giordano and M. Antonietti, Angew. Chem., Int. Ed., 2012, 124, 11910–11914.
20. Q. S. Gao, C. Giordano, M. Antonietti, Angew. Chem. Int. Ed., 2012, 51, 11740.
21. K. Chang and W. X. Chen, ACS Nano, 2011, 5, 4720–4728.
22. Y. C. Liu, L. F. Jiao, Q. Wu, J. Du, Y. P. Zhao, Y. C. Si, Y. J. Wang and H. T. Yuan, J. Mater. Chem. A, 2013, 1, 5822–5826.
23. C. Q. Feng, J. Ma, H. Li, R. Zeng, Z. P. Guo, H. K. Liu, Mater. Res. Bull., 2009, 44, 1811.
24. M. L. Mao, L. Mei, D. Guo, L. C. Wu, D. Zhang, Q. H. Li and T. H. Wang, Nanoscale, 2014, 6, 12350-12353.
25. X. Xu, Z. Y. Fan, S. J. Ding, D. M. Yu and Y. P. Du, Nanoscale, 2014, 6, 5245.
26. C. C. Wang and J. Y. Ying, Chem. Mater., 1999, 11, 3113.
27. R. L. Penn and J. F. Banfield, Geochim. Cosmochim. Acta, 1999, 63, 1549.
28. J. X. Qiu, P. Zhang, M. Ling, S. Li, P. Liu, H. J. Zhao and S. Q. Zhang, ACS Appl. Mater. Interfaces, 2012, 4, 3636.
29. G. Lee, H. G. Yan, L. E. Brus, T. F. Heinz, J. Hone and S. Ryu,ACS Nano, 2010, 4, 2695.
30. H. Li, Q. Zhang, C. C. R. Yap, B. K. Tay, T. H. T. Edwin,A. Oliver and D. Baiwargeat, Adv. Funct. Mater., 2012, 22,1385.
31. Y. C. Liu, L. F. Jiao, Q. Wu, Y. P. Zhao, K. Z. Cao, H. Q. Liu, Y. J. Wang and H. T. Yuan, Nanoscale, 2013, 5, 9562.
32. C. Y. Xu, P. X. Zhang and L. Yan, J. Raman Spectrosc., 2001, 32,862.
33. J. Z. Li, K. Yu, Y. H. Tan, H. Fu, Q. F. Zhang, W. T. Cong, C. Q. Song, H. H. Yin and Z. Q. Zhu, Dalton Trans., 2014, 43, 13136
34. L. Yang, X. Cui, J. Zhang, K. Wang, M. Shen, S. Zeng, S. A. Dayeh, L. Feng and B. Xiang, Sci. Rep., 2014, DOI: 10.1038/srep05649.
35. B. J. Morgan, D. O. Scanlon and G. W. Watson, J. Mater. Chem., 2009, 19, 5175–5178.
36. S. J. Ding, J. S. Chen and X. W. Lou, Chem.–Eur. J., 2011, 17, 13142.
37. X. Jiang, X. L. Yang, Y. H Zhu, H. L. Jiang, Y. F. Yao, P. Zhao and C. Z. Li., J. Mater. Chem. A, 2014, 2, 11124.
38. H. B. Wang, C. J. Zhang, Z. H. Liu, L. Wang, P. X. Han, H. X. Xu, K. J. Zhang, S.M. Dong, J. H. Yao and G. L. Cui, J. Mater. Chem., 2011, 21, 5430.
39. K. Chang and W. Chen, Chem. Commun., 2011, 47, 4252.
40. S. J. Ding, D. Zhang, J. S. Chen and X. W. Lou, Nanoscale, 2012, 4, 95.
41. H. J. Zhou, L. Liu, X. C. Wang, F. X. Liang, S. J. Bao, D. M. Lv,Y. K. Tang and D. Z. Jia, J. Mater. Chem. A, 2013, 1, 8525.
42. Y. Miki, D. Nakazato, H. Ikuta, T. Uchida, M. Wakihara, J. Power Sources, 1995, 54, 508.
43. J. Xiao, X. J. Wang, X. Q. Yang, S. D. Xun, G. Liu, P. K. Koech, J. Liu, J. P. Lemmon, Adv. Funct. Mate., 2011, 21, 2840.
44. Q. Wang, J. H. Li, J. Phys. Chem. C 2007, 111, 1675.
45. X. P. Fang, X. Q. Yu, S. F. Liao, Y. F. Shi, Y. S. Hu, Z. X. Wang, G. D. Stucky, L. Q. Chen, Mesoporous Mater., 2012, 151,418.
46. X. H. Cao, Y. M. Shi, W. H. Shi, X. H. Rui, Q. Y. Yan, J. Kong and H. Zhang, Small, 2013, 9, 3433–3438.
47. T. Stephenson, Z. Li, B. Olsen and D. Mitlin, Energy Environ. Sci., 2014, 7, 209.
48. P. L. Sun, W. X. Zhang, X. L. Hu, L. X. Yuan and Y. H. Huang., J. Mater. Chem. A, 2014, 2, 3498.
49. P. R. Bueno and E. R. Leite, J. Phys. Chem. B, 2003, 107, 8868.

# Graphical Abstract

Firework-shaped $TiO_2$ microspheres embedded with few-layer $MoS_2$ are prepared by a novel strategy, and the composite electrode exhibits excellent cycling performance, high capacity and rate capability compared to pure $MoS_2$ and $TiO_2$ electrode.